NASA TT F-11,907

INVESTIGATION OF THREE-DIMENSTIONAL DESCENT TRAJECTORIES OF LIFTING RE-ENTRY VEHICLES

W. Hein, F. Mysliwetz, and F. Oppelt

Translation of: "Untersuchung von dreidimensionalen Abstiegsbahnen für auftriebserzeugende Raumflugkörper." Bundesministerium für Wissenschaftliche Forschung, West Germany, Report BMwF-FB-W-67-28, Munich, September 1967. 30 p.

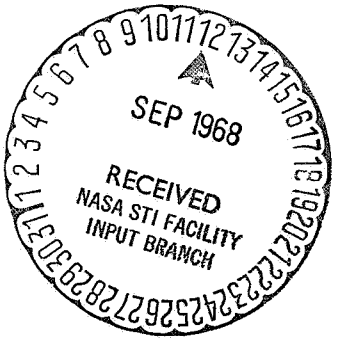

NATIONAL AERONAUTICS AND SPACE ADMINISTRATION
WASHINGTON, D.C. SEPTEMBER 1968

INVESTIGATION OF THREE-DIMENSIONAL DESCENT TRAJECTORIES OF LIFTING RE-ENTRY VEHICLES

W. Hein, F. Mysliwetz, and F. Oppelt

ABSTRACT: For the second stage of an aerospace transport, descent trajectories and footprints have been determined at various banking angles and lift-drag ratios. The maximum longitudinal range that can be obtained under the assumptions made in this investigation amounts to 3/4 of the earth's equator, whereas a maximum cross range of 60° can be reached. Temperatures on the lower surface of the wing and at the stagnation point are about 150-200° K higher for the banked-entry maneuvers than for corresponding plane trajectories. Normal accelerations, though higher, remain under 3 G.

/4

CONTENTS

/5

1. Introduction 3

2. Symbols 4

3. Theoretical Principles 6

3.1 Area Investigated 6

3.2 System of Equations 6

4. Results 7

4.1 Footprints 7

4.2 Aerodynamic Heating 9

4.3 Mechanical Stress 10

5. References 10

1. INTRODUCTION

For reusable re-entry systems to link the surface of the earth and objects in orbit in regular flight, it is essential that upon their return from orbit they should be able to land at an airport. In contrast to ballistic space vehicles (Mercury capsule, Gemini, etc.) whose landing points on earth are mainly dependent on the position and magnitude of the braking impulse in orbit, reuseable systems require greater maneuverability within the atmosphere. After re-entry, the possibility must exist for landing at various landing areas. Three-dimensional descent trajectories within the atmosphere were computed with the aid of a digital computer [1] for constant entry conditions, and the following trajectory concepts were investigated. /6*

(a) Flights with optimal lift-drag ratios to attain distance ranges as large as possible. Some of the investigated paths were flown with constant banking angles, while others, after attainment of a predetermined azimuth angle, were shifted to straight-line flight from curvilinear flight at a constant angle.

(b) Paths with constant lift-drag ratios ($\varepsilon = 1$) corresponding to a large angle of incidence (40°) with constant banking angles. These trajectories are more favorable with regard to aerodynamic heating and mechanical stress and, owing to their shorter ranges, are closest to the requisite practical case. Broader control concepts (e.g., avoidance of orbit oscillation) are outside the scope of this investigation.

---

*Numbers in margin indicate pagination in original foreign text.

2. SYMBOLS

A	[kp]	Aerodynamic lift	/7
c_f	[-]	Friction factor f (Re*)	
g	[m/s^2]	Gravitational acceleration	
H	[km]	Flight altitude	
H_s	[kcal/kg]	Enthalpy of the air after impact	
h_w	[kcal/kg]	Enthalpy of the air at wall temperature	
$h_{w\,300}$	[kcal/kg]	Reference entalpy at 300° K	
l	[m]	Vehicle length	
m	[kp s^2/m]	Vehicle mass	
p	[kp/m^2]	Pressure	
Pr*	[-]	Prandtl number	
r	[m]	Radius	
Re	[-]	Reynolds number $Re^* = \frac{v_\delta \cdot l}{\nu^*}$	
r_N	[m]	Leading-edge radius	
S	[kp]	Thrust	
T*	[°K]	Reference temperature	
v	[m/s]	Velocity	
W	[kp]	Aerodynamic resistance	
α	[°]	Angle of attack	
β	[°]	Sideslip angle	
γ	[°]	Flight path angle	
ε	[°]	Lift-drag ratio	
ε	[-]	Radiation factor $f(T_w)$	
λ	[°]	(Geographic) latitude	
λ^*	[kg/m·s]	Thermal viscosity $f(p_\delta, T^*)$	
μ	[°]	Banking angle	/8
ν^*	[m^2/s]	Kinematic viscosity $f(p_\delta, T^*)$	
τ	[°]	Geographic longitude	
ρ	[$kp \cdot s^2/m^4$]	Air density, ρ_{SL} density at altitude above sea level	
χ	[°]	Azimuth angle.	

Indices

x_f)	
y_f)	References to fixed body coordinates
z_f)	
δ	Boundary layer edge
w	Wall
r	Recovery
∞	External flow

3. THEORETICAL PRINCIPLES

3.1. Area Investigated

The conditions of entry into the atmosphere were kept constant /9 corresponding to a braking impulse of 3% of the orbital mass at an altitude of 300 km:

Altitude	120 km
Velocity	7817 m/sec
Position angle	-1.78°

(a) Paths with optimal lift-drag ratios:
(Lift-drag ratio as a function of Mach number and altitude)

1. Curvilinear flights

   Banking angle constant: $\mu = 0, 30, 45, 60°$.

2. Curvilinear flight with subsequent straight-line flight

   Banking angle constant: $\mu = 30, 45, 60°$.
   After attaining a change of direction of $\chi = 45, 90$, and $135°$, subsequent straight-line flight with $\mu = 0°$.

(b) Paths with constant lift-drag ratio ($\varepsilon = 1$)
Curvilinear flight only with constant banking angle:

$\mu = 0, 30, 45, 60°$.

The space vehicle used in the investigations is shown in Fig. 15.

3.2 System of Equations

The equations for the three-dimensional descent trajectories are derived in detail in [1]. They need only be mentioned here. They are valid for a spherical, nonrotating earth. The space ve- /10 hicle will be treated as a mass point.

$$\dot{v} = -\frac{W}{m} - g\sin\gamma + \frac{1}{m}\left(S_{xf}\cos\alpha\cos\beta - S_{yf}\sin\beta + S_{zf}\sin\alpha\cos\beta\right)$$

$$\dot{\chi} = g\frac{\operatorname{tg}\mu}{v} + \frac{1}{mv\cos\gamma\cos\mu}\left(S_{xf}\cos\alpha\sin\beta + S_{yf}\cos\beta + S_{zf}\sin\alpha\sin\beta\right)$$

$$-\frac{v}{r}\operatorname{tg}\mu - \frac{v}{r}\cos\gamma\cos\chi\operatorname{tg}\lambda + \dot{\gamma}\frac{\operatorname{tg}\mu}{\cos\gamma}$$

$$\dot{\gamma} = -\frac{1}{mv\cos\mu}\left(-A - S_{xf}\sin\alpha + S_{zf}\cos\alpha\right) - g\frac{\cos\gamma}{v} +$$

$$+\frac{v}{r}\cos\gamma - \cos\gamma\, tg\mu\left(\frac{v\cos\chi\, tg\lambda}{r}\cos\gamma + \dot{\chi}\right)$$

$$\dot{t} = \frac{v\cos\gamma\cos\chi}{r\cos\lambda}$$

$$\dot{\lambda} = \frac{v\cos\gamma\sin\chi}{r}$$

$$\dot{r} = v\sin\gamma$$

4. RESULTS

4.1. Footprints

/11

Landing areas for re-entering lift-producing space vehicles are presented in Figs. 1-6. Calculations were carried out for orbit paths from 120 km to below 20 km in altitude, with the assumption of a nonrotating earth. Except for the flight outside the atmosphere, an equatorial orbital plane was assumed (see Fig. 1).

Footprints for a constant banking angle are shown in Fig. 2. We see from this figure that the paths flown with the most effective lift-drag ratios yield very large distance ranges. We were able to realize maximal longitudinal ranges of 270° of geographic longitude and maximal latitudinal ranges of 55° of geographic latitude. One can also (with less than optimal lift-drag ratios) locate still other possible landing points within the boundary line.

For combinations of curvilinear and straight-line flight, suitable landing zones are shown in Figs. 3-5. These flight paths were first flown with constant banking angle; upon attaining a certain azimuth angle (45, 90, and 135°), the banking was suddenly stopped and straight-line flight began. The largest footprints were yielded in this mode when a straight-line flight was begun after a 90° change of direction. Latitudinal ranges of up to nearly 70° were thus obtained.

Since the paths flown with optimal lift-drag ratios (ε_{opt} = 1.7→2.5, α_{opt} = 10°→20°) give very large footprints, paths which were flown with a constant lift-drag ratio ε = 1 and a high angle of attack (α=40° were also investigated. Fig. 2 shows a footprint for paths with constant banking. The maximal logitudinal and latitudinal range is essentially smaller, but corresponds in order of magnitude to the size of continents. This dimensional expansion of the landing points agreed approximately with the practical requirements of the space-vehicle stages returning from orbit.

The descent trajectories investigated here show no stationary glide, but exhibit oscillating characteristics (see Fig. 14). With re-entry paths to be executed in practice, however, the banking angle and angle of attack would be modified so that the oscillation could be stabilized. /12

A comparison of the above results with the footprints of the Dyna-Soar [2] shows that the order of magnitude of the maximal longitudinal and latitudinal ranges are in agreement. The comparative values are given in the following table.

	Maximal longitudinal range	Maximal latitudinal range	Lift-drag ratio
Space Transporter, second stage	29,640	6,000	Optimal value about 2.2 on the average
Dyna-Soar	25,000	7,800	3.0
Space Transporter, second stage	9,660	900	1.0
Dyna-Soar	8,300	1,100	1.0

The smaller longitudinal ranges for the Dyna-Soar as opposed to those of the "Space Transporter" (German: "Raumtransporter"... ...Translator's note) are caused by the rotation of the earth. The difference in the latitudinal distance ranges with high lift-drag ratios is to be attributed to the different lift-drag ratios. The results given in [3] should be included in a broader comparison.

We looked for three-dimensional re-entry paths to obtain maximum latitudinal distance ranges. For constant lift-drag ratios, latitudinal distance ranges were obtained which were somewhat lower than those calculated here. With a lift-drag ratio of 2.5, the maximal latitudinal distance range amounted to 5500 km (entry conditions: h_0 = 100 km, v_0 = 7700 m/sec, γ_0 = -3°). It is interesting that for the optimal flight program, banking decreased with flight altitude. /13

High aerodynamic efficiency, therefore, permits one to obtain footprints which cover a large portion of the earth. With lower aerodynamic efficiency (ε = 1, larger angle of attack, smaller ballistic factor), one can attain ranges of the order of magnitude of continents.

Lift-drag ratio

4.2. Aerodynamic Heating

Re-entering space vehicles, due to their high flight velocity, are exposed to severe compressional and frictional heating. Therefore, for the flight paths considered here, the maximal wall temperatures at the stagnation point and on the underside of the wing were determined.

The heat flux at the stagnation point was calculated from the Fay-Riddell formula [5]:

$$\dot{q}_w = \frac{38,703}{\sqrt{r_N}} \cdot \left(\frac{v_\infty}{10^3}\right)^{3,15} \sqrt{\frac{\rho_\infty}{\rho_{SL.}}} \cdot \frac{H_s - h_w}{H_s - h_{w300^\circ}} \quad [\text{kcal/m}^2 \cdot \text{s}]$$

For the average heat flux on the underside of the space vehicle, which one can approximate as a flat surface of length l (*m*), we obtain:

$$\dot{q}_w = \frac{1}{2} \cdot c_f \cdot Re^* \cdot Pr^{*\frac{1}{3}} \cdot \frac{\lambda^*}{l} \cdot (h_r - h_w); \quad [\text{kcal/m}^2 \cdot \text{s}] \quad [6]$$

Using the heat flux, we then determine the wall temperature with the expression for radiation equilibrium:

$$T_w = 519,045 \cdot \sqrt[4]{\frac{\dot{q}_w}{\varepsilon}}; \quad [^\circ K]$$

Figures 7-10 show plots of wall temperature against flight velocity for different banking angles and lift-drag ratios. As a rule, the temperatures for curvilinear flights are higher than those for corresponding straight-line flights. This is due to the fact that, in banked flight, dense atmospheric layers are reached more quickly and at higher speeds. Moreover, it is shown that paths flown with a large angle of attack $\alpha = 40^\circ$ (lift-drag ratio $\varepsilon = 1$) produce considerably lower temperatures than the former with maximal lift-drag ratio. The maximal difference for the stagnation point amounts to about 500° K, while that for the underside of the wing amounts to 100° K. Since the temperature considered permissible for metal skins (1200°K) will be exceeded on the underside of the wing, the walls must have an ablation shield. /14

The data given in Figures 7-10 present the temperature maxima which are produced from apogee to apogee of an oscillating orbit. The broken like joining these points, therefore, does not represent the temperature vs. velocity curve, but rather the contour of the temperature maxima.

4.3. Mechanical Stress

The maximal normal accelerations (safe load factors) are given in Figs. 11 and 12. A stress limit of 3 g is attained for the largest banking angle ($\mu = 60°$) in flights with optimal lift-drag ratios, and will be exceeded somewhat in the combination of curvilinear and straight-line flights. For lift-drag ratios of $\varepsilon = 1$, the stresses remain under 2 g throughout. Curvilinear flights after re-entry present no difficulties with regard to mechanical stress.

Figure 13 gives the time curve of the safe load factor for orbits with different banking angles.

REFERENCES

1. Engler, Liu.: Ausgangsgleichungen zum Rechnen dreidimensionaler Aufstiegsbahnen. (Initial Equations for the Calculation of Three-Dimensional Launching Trajectories.) Junkers-Bericht No. 064-172, 1964. /15
2. Yoler, J.A.: Dyna-Soar. Aero Space Eng., August, 1961.
3. Wagner: Roll Modulation for Maximum Re-entry Lateral Range. AIAA Paper No. 64-471,1964.
4. Hein and Mysliwetz: Untersuchung von dreidimensionalen Abstiegsbahnen fur auftriebserzeugende Raumflugkörper. (Investigation of Three-Dimensional Descent Trajectories for Lift-Producing Space Vehicles). Junkers-Bericht No. 066-227, 1966.
5. Fay and Riddell: Theory of Stagnation Point Heat Transfer in Dissociated Air. J. Aeronaut. Sci. Vol. 25, No. 2, Feb.,1958.
6. Eckert, E.R.G.: Engineering Relations for Friction and Heat Transfer to Surfaces in High Velocity Flow. J. Aeronaut. Sci., No. 8, August, 1955.

Translated for the National Aeronautics and Space Administration by:
Aztec School of Languages, Inc.
Research Translation Division (532)
Acton, Massachusetts.
NASw-1692

/16

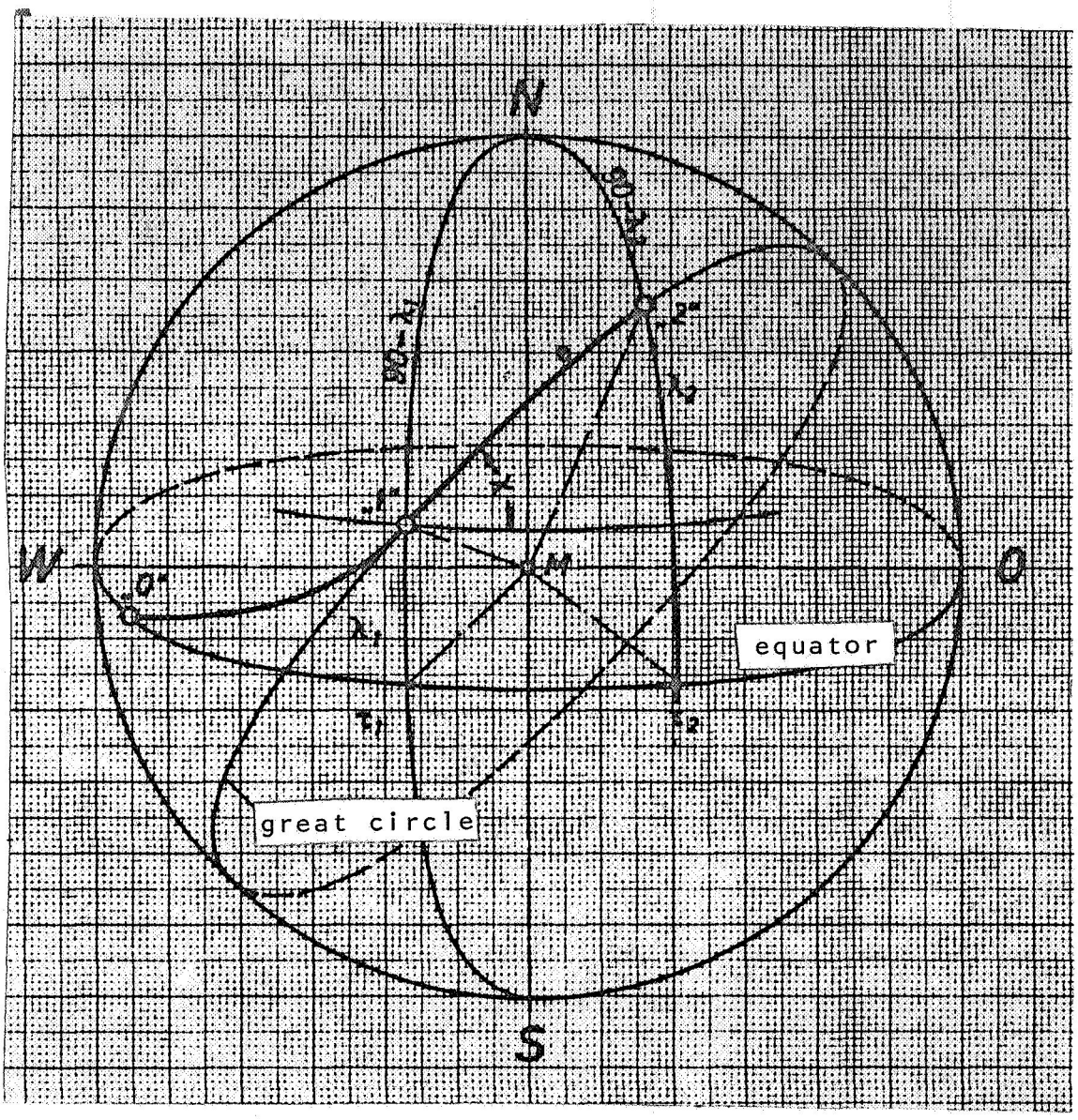

"0" Equatorial entry into the atmosphere

1 Endpoint of curb curvilinear flight = beginning of straight line flight

2 Endpoint of descent trajectory at altitude = 20 km

Figure 1. Basic Diagram

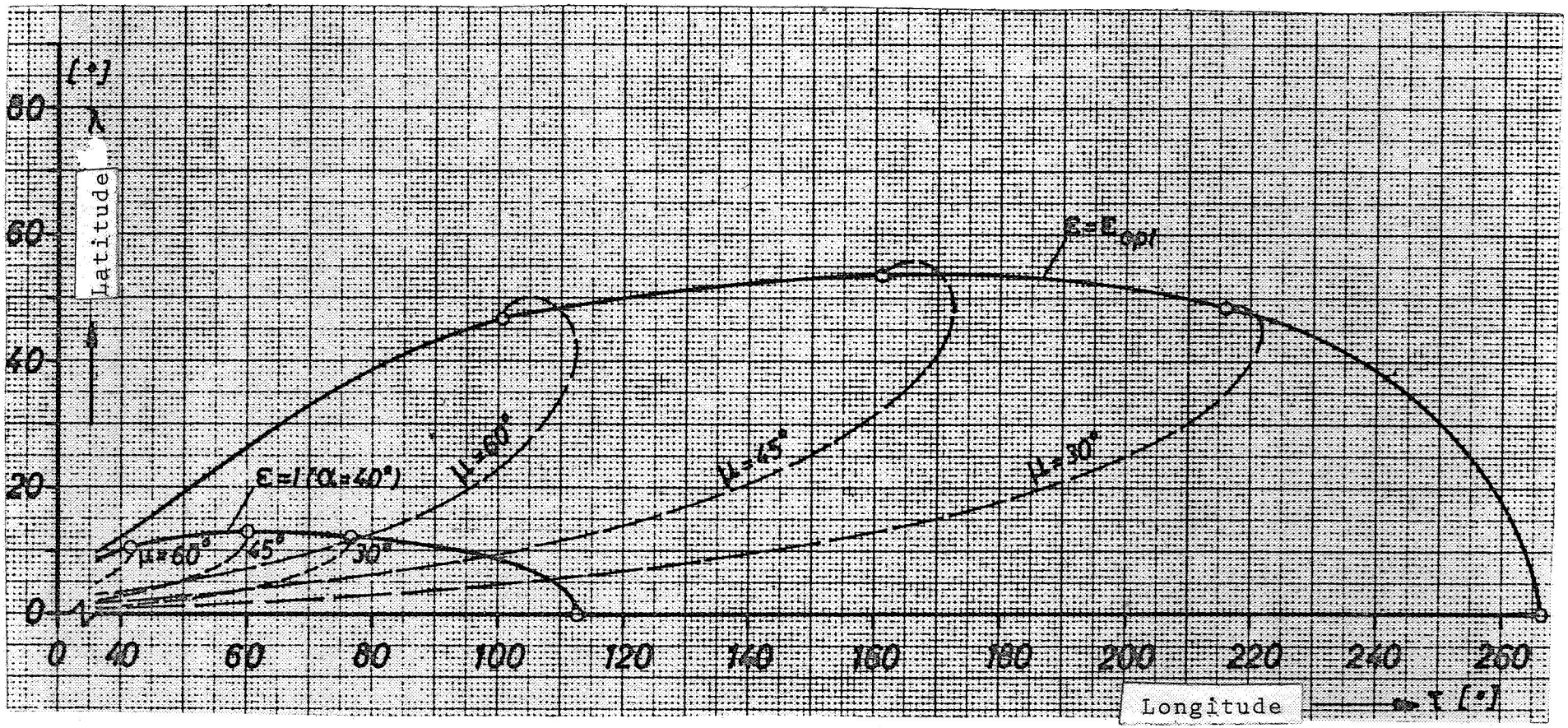

Figure 2. Footprint with Constant Banking μ=const. from 120 to 20 km altitude.

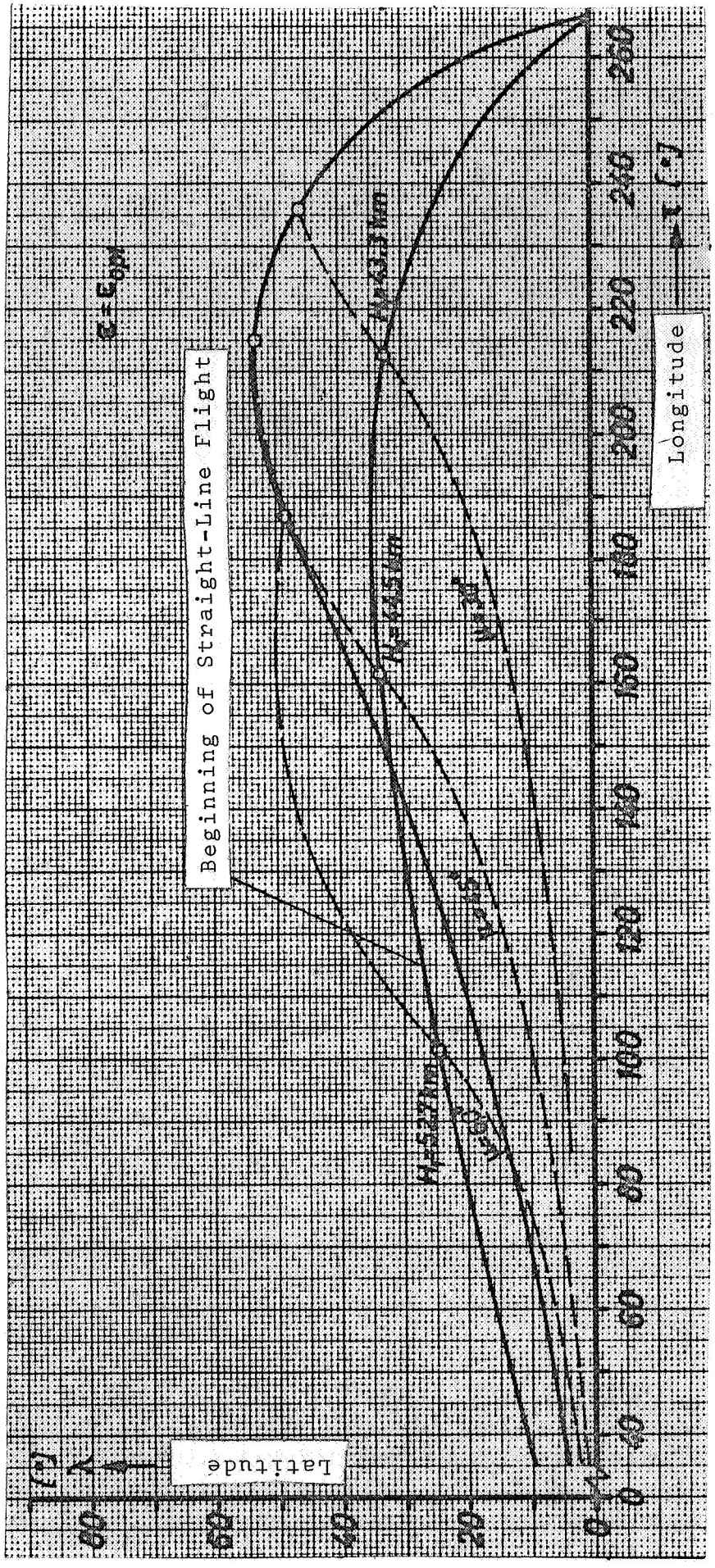

Figure 3. Footprint for Direction Change of 45°

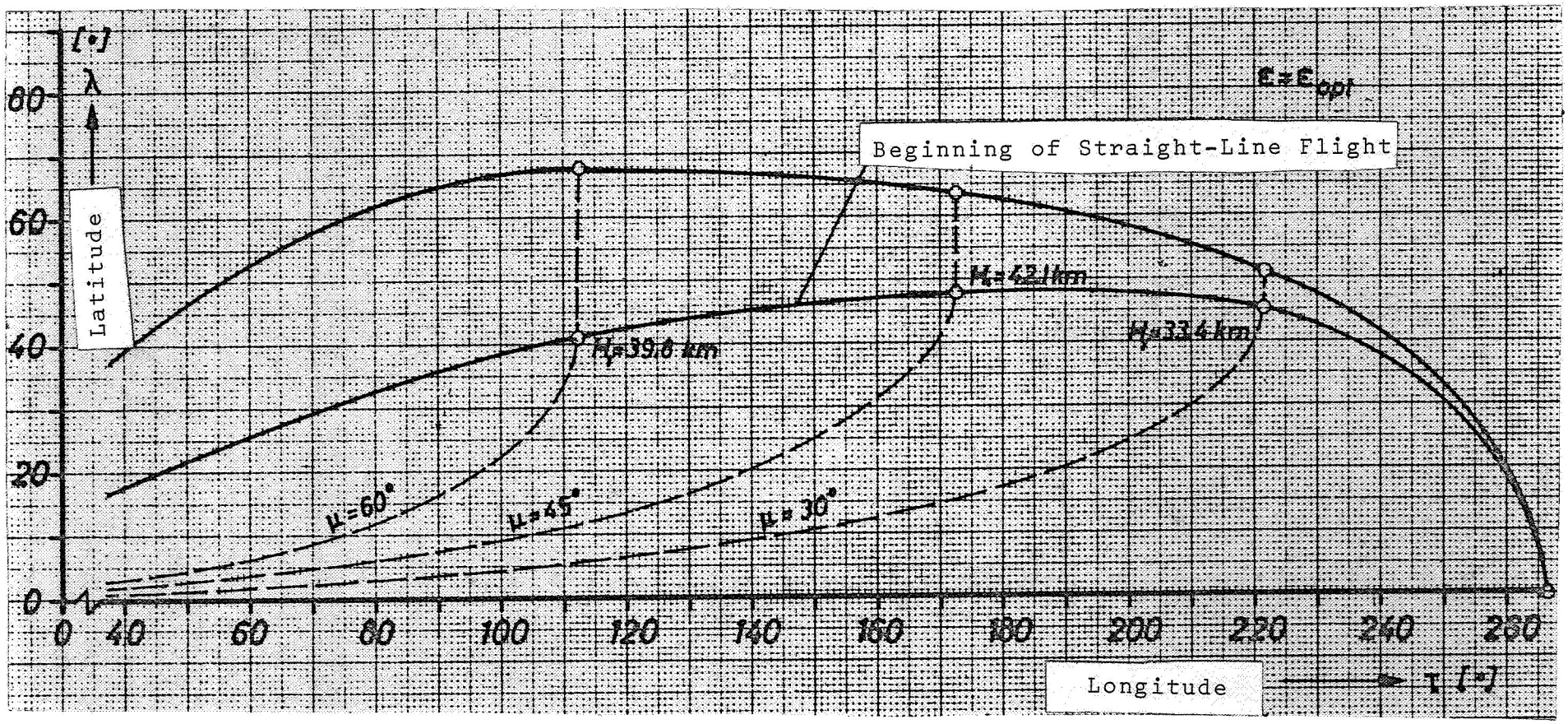

Figure 4. Footprint for Direction Change of 90°

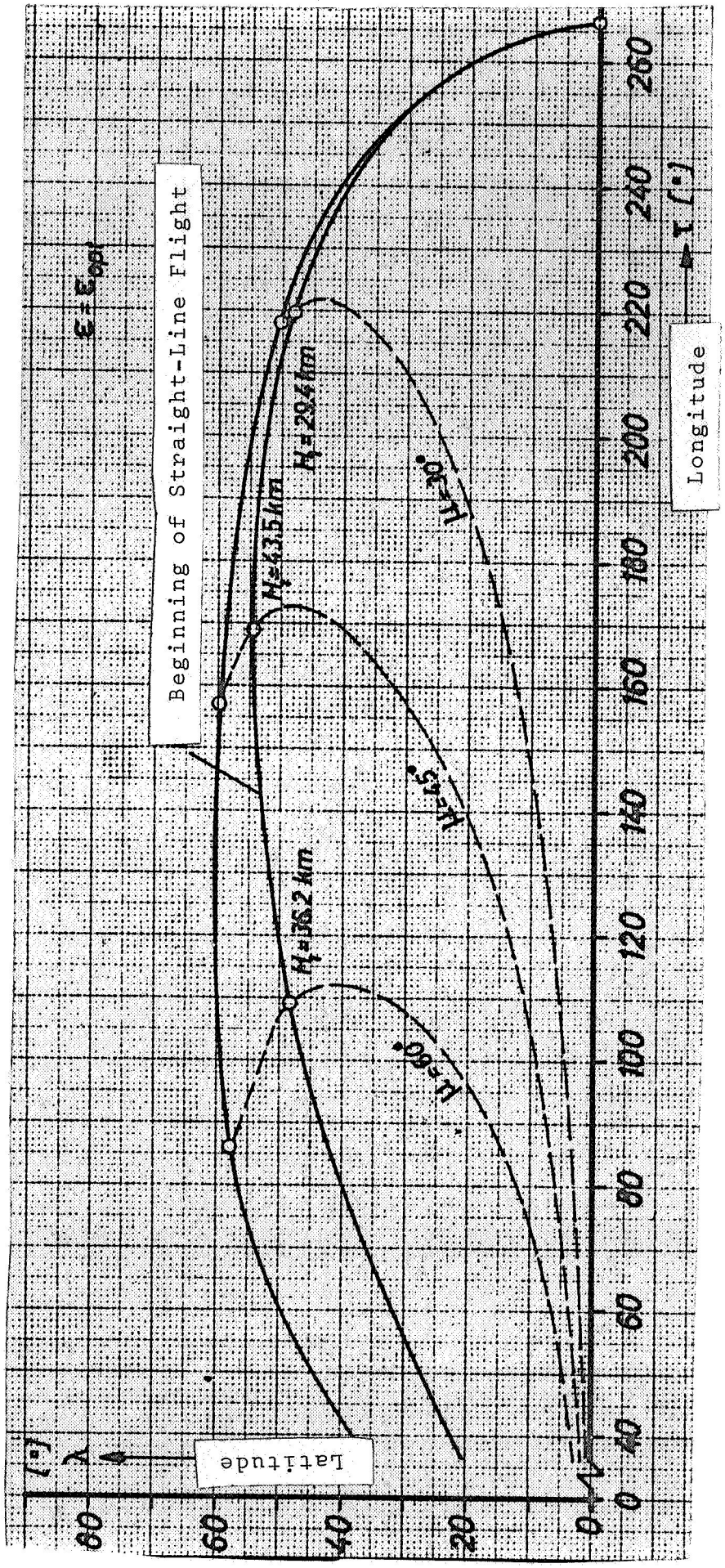

Figure 5. Footprint for Direction Change of 135°

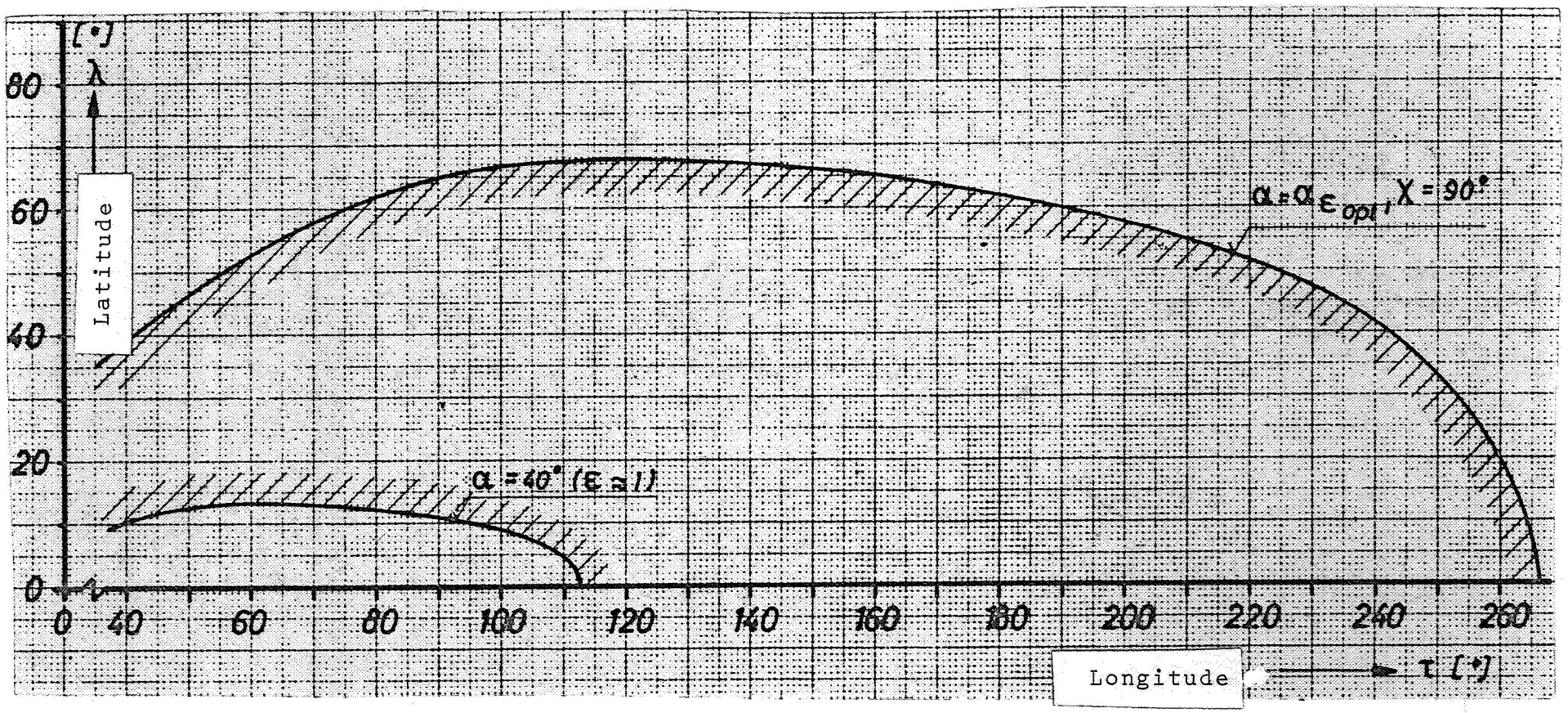

Figure 6. Maximal Landing Area

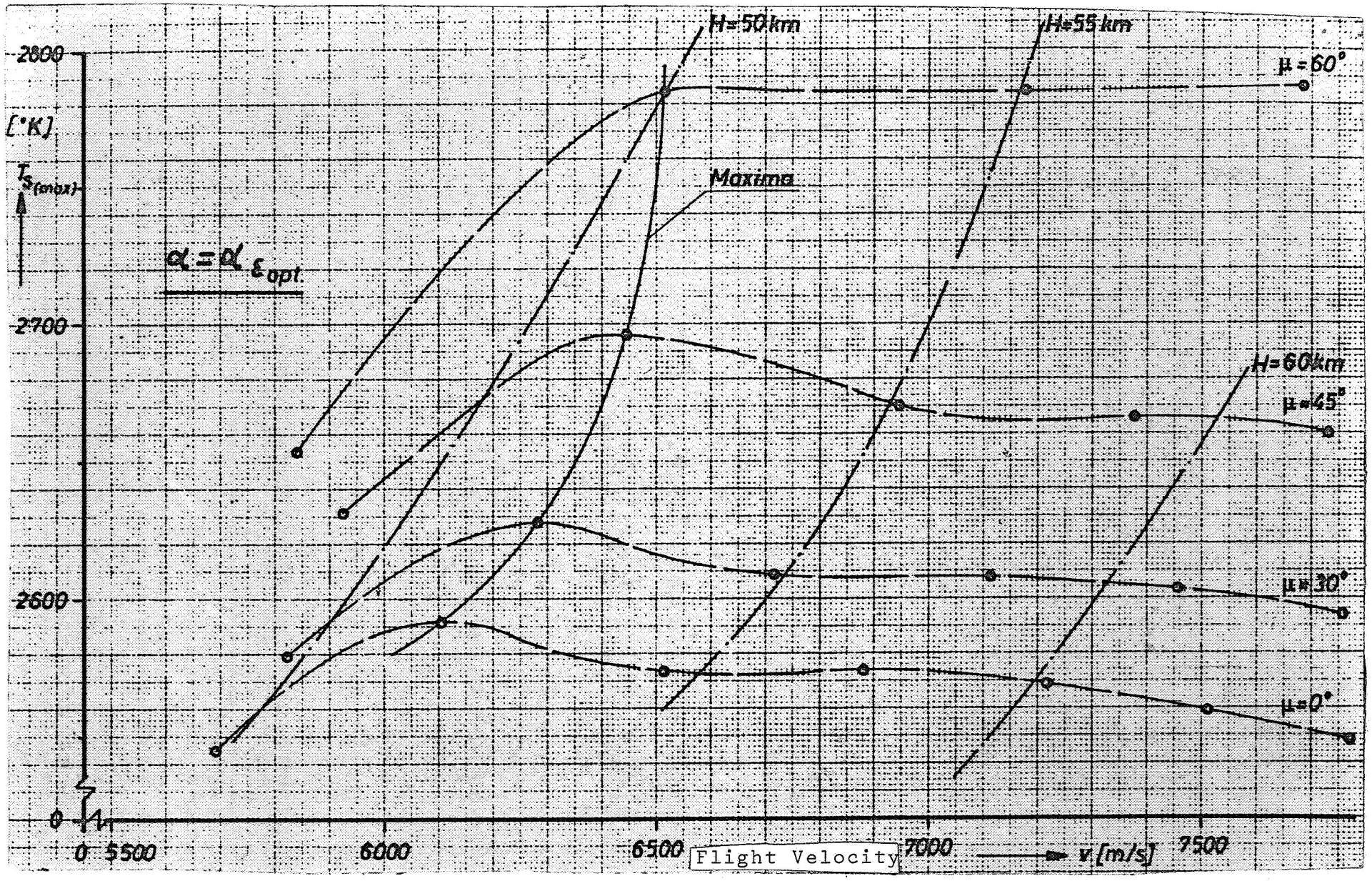

Figure 7. Stagnation-Point Heating

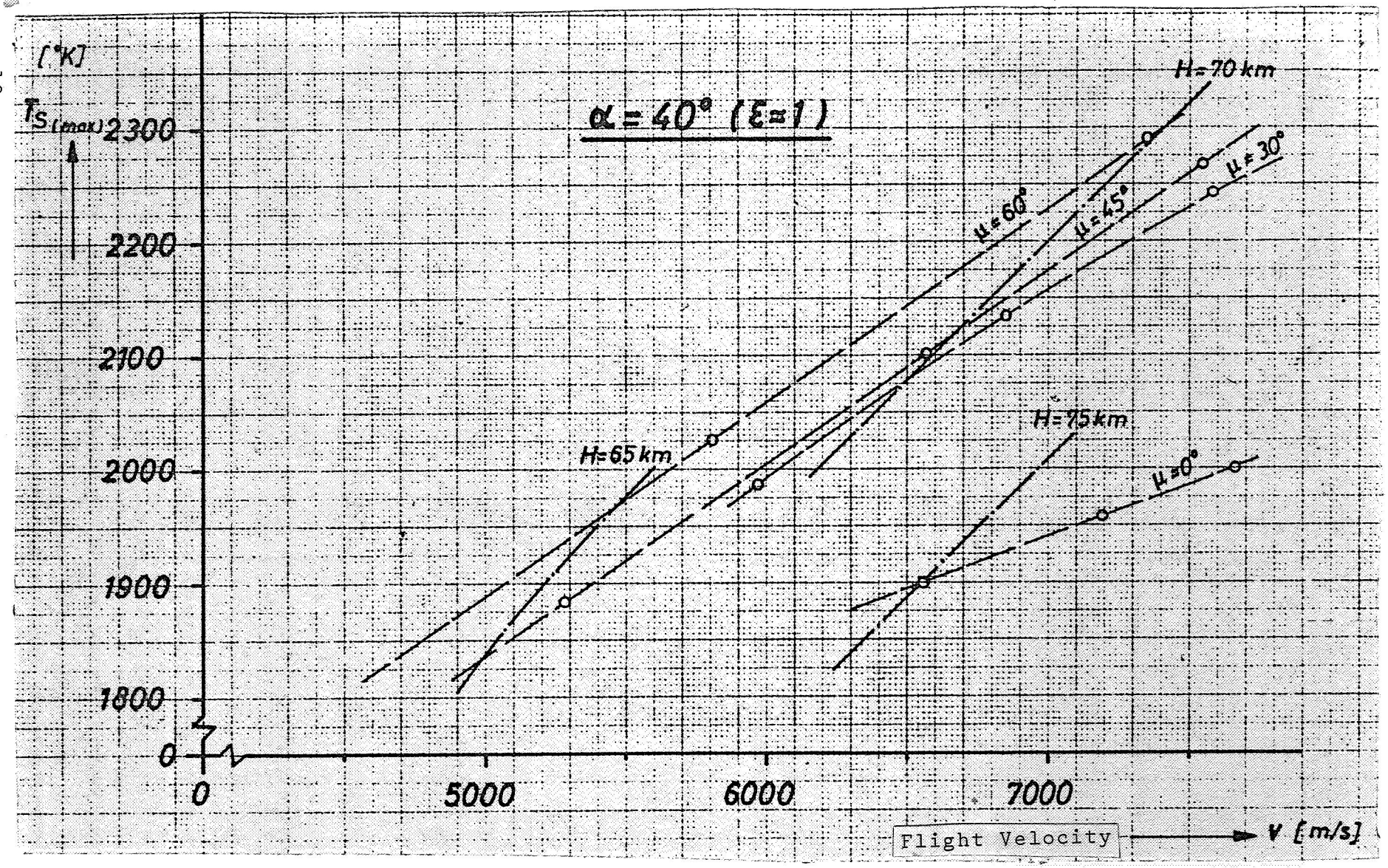

Figure 8. Stagnation-Point Heating

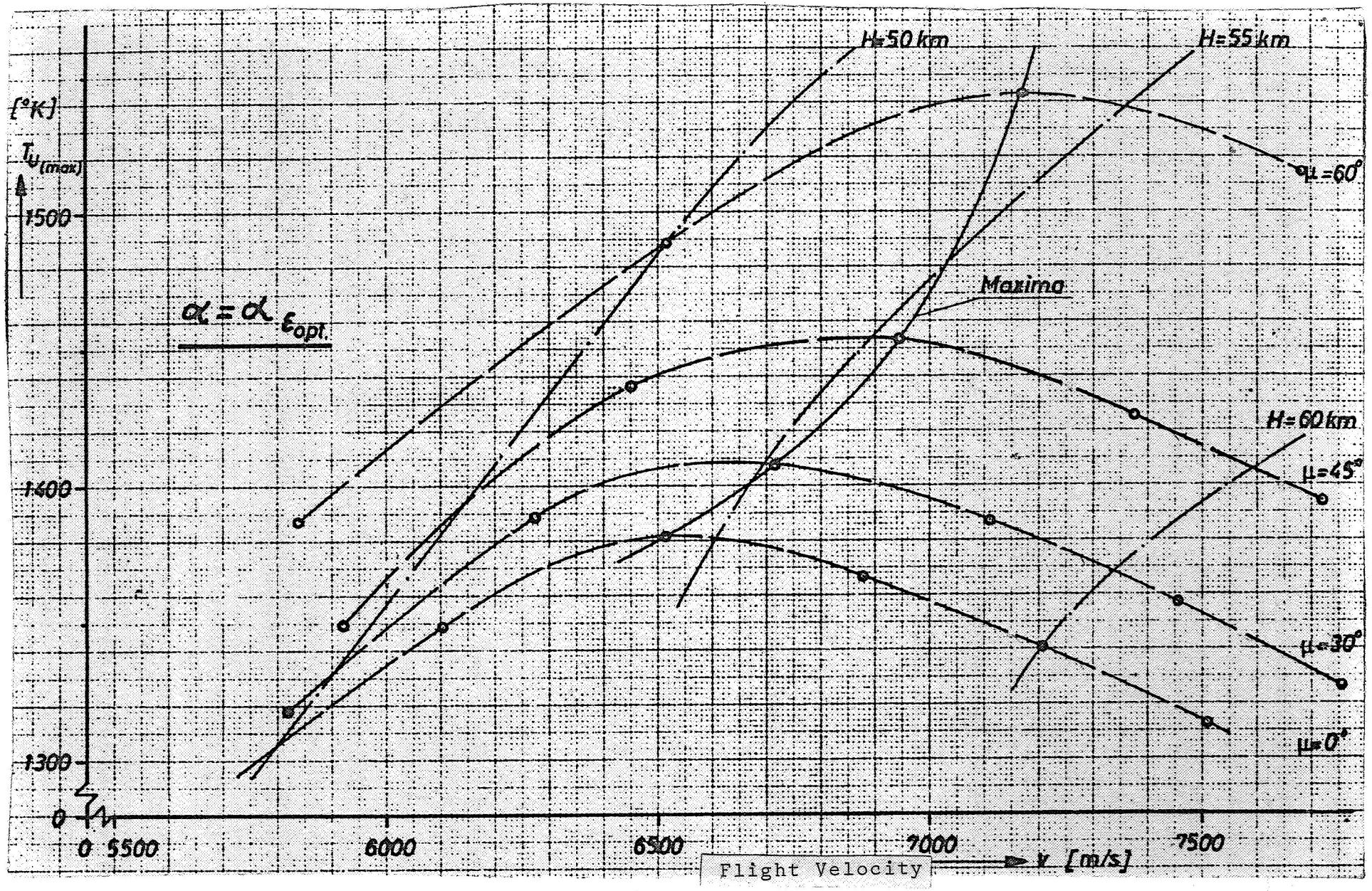

Figure 9. Average Temperature of Underside of Wing (Maximal Values)

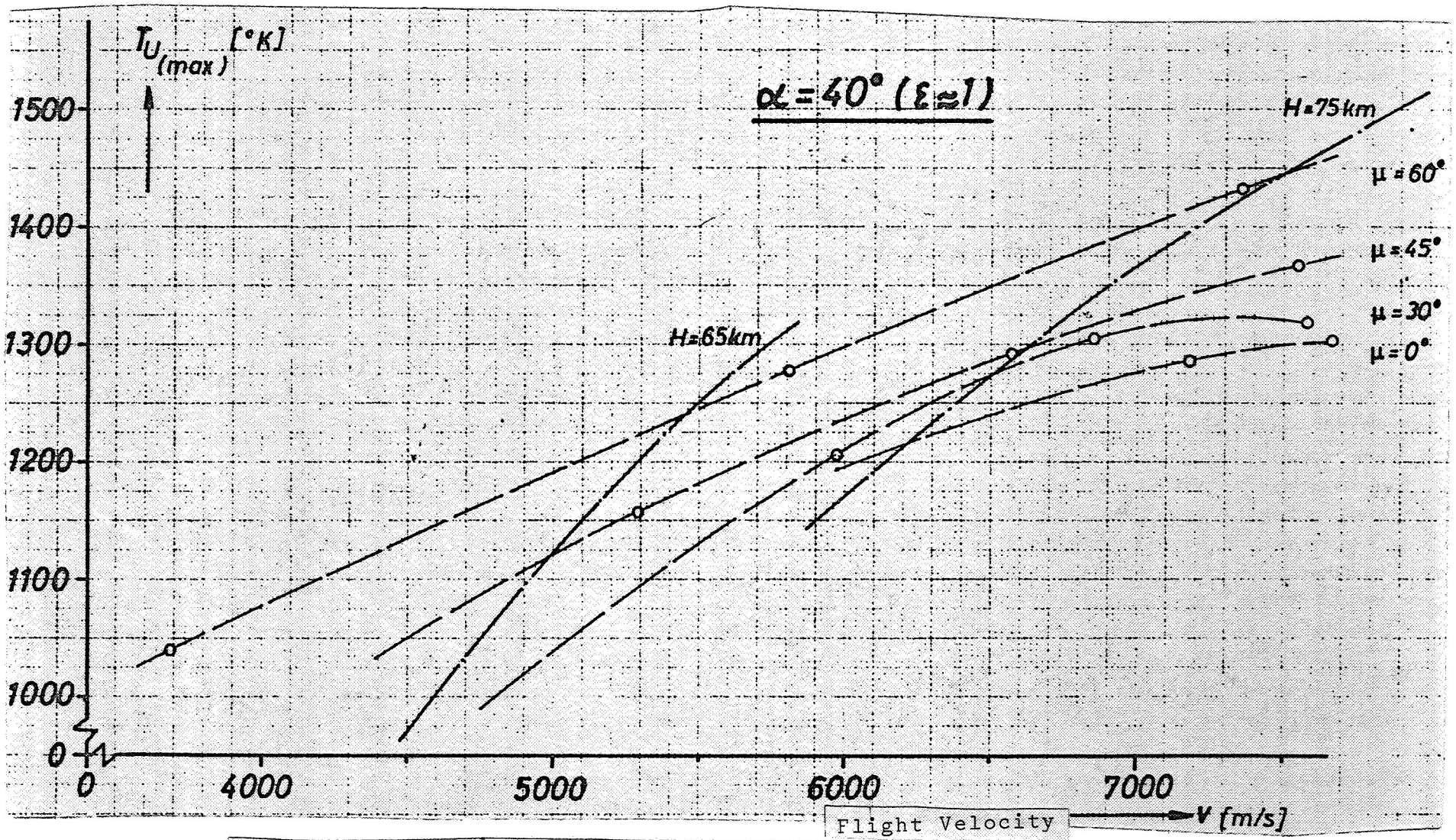

Figure 10. Average Temperature of Underside of Wing (Maximal Values)

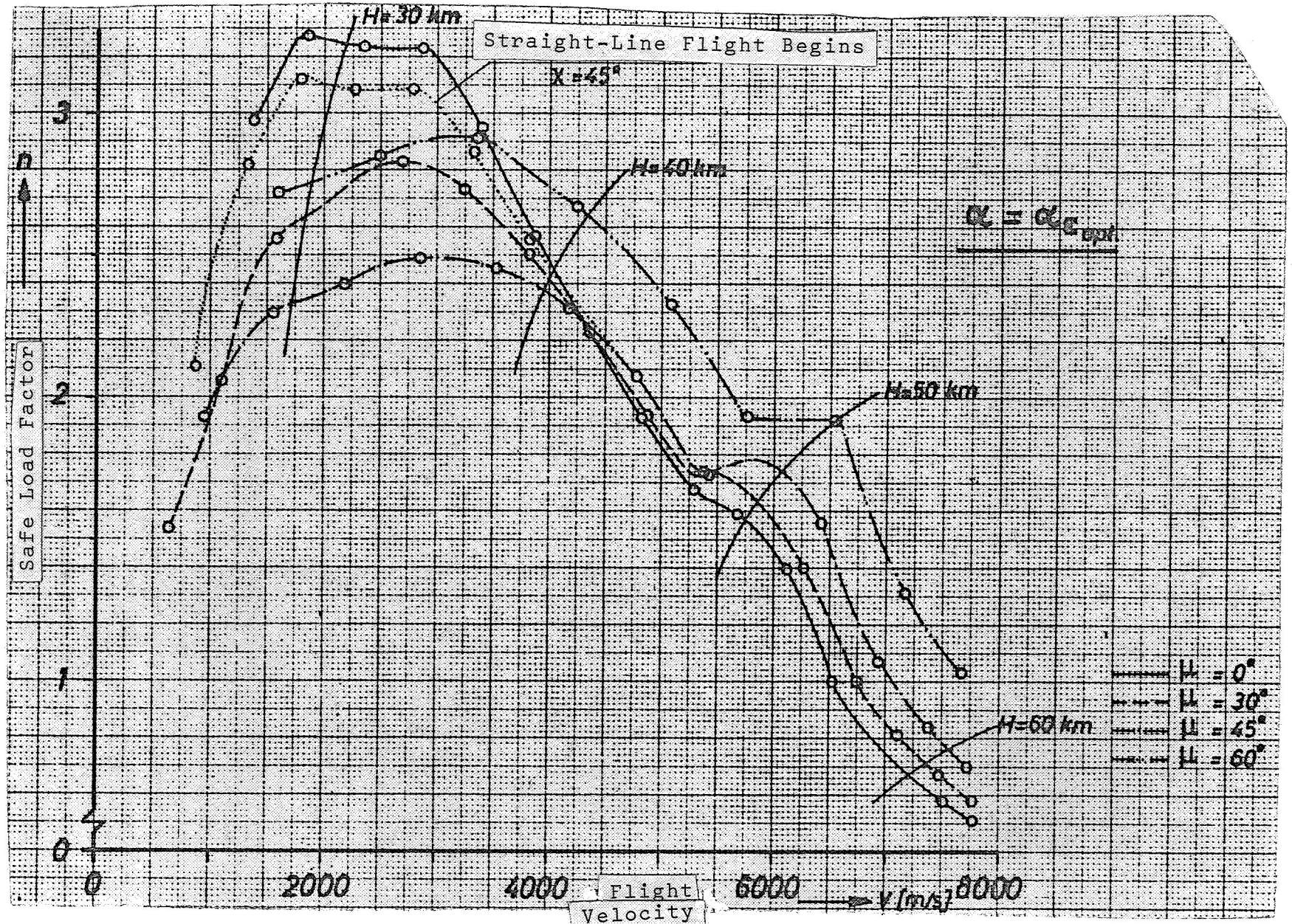

Figure 11. Safe Load Factor (Normal to Path)

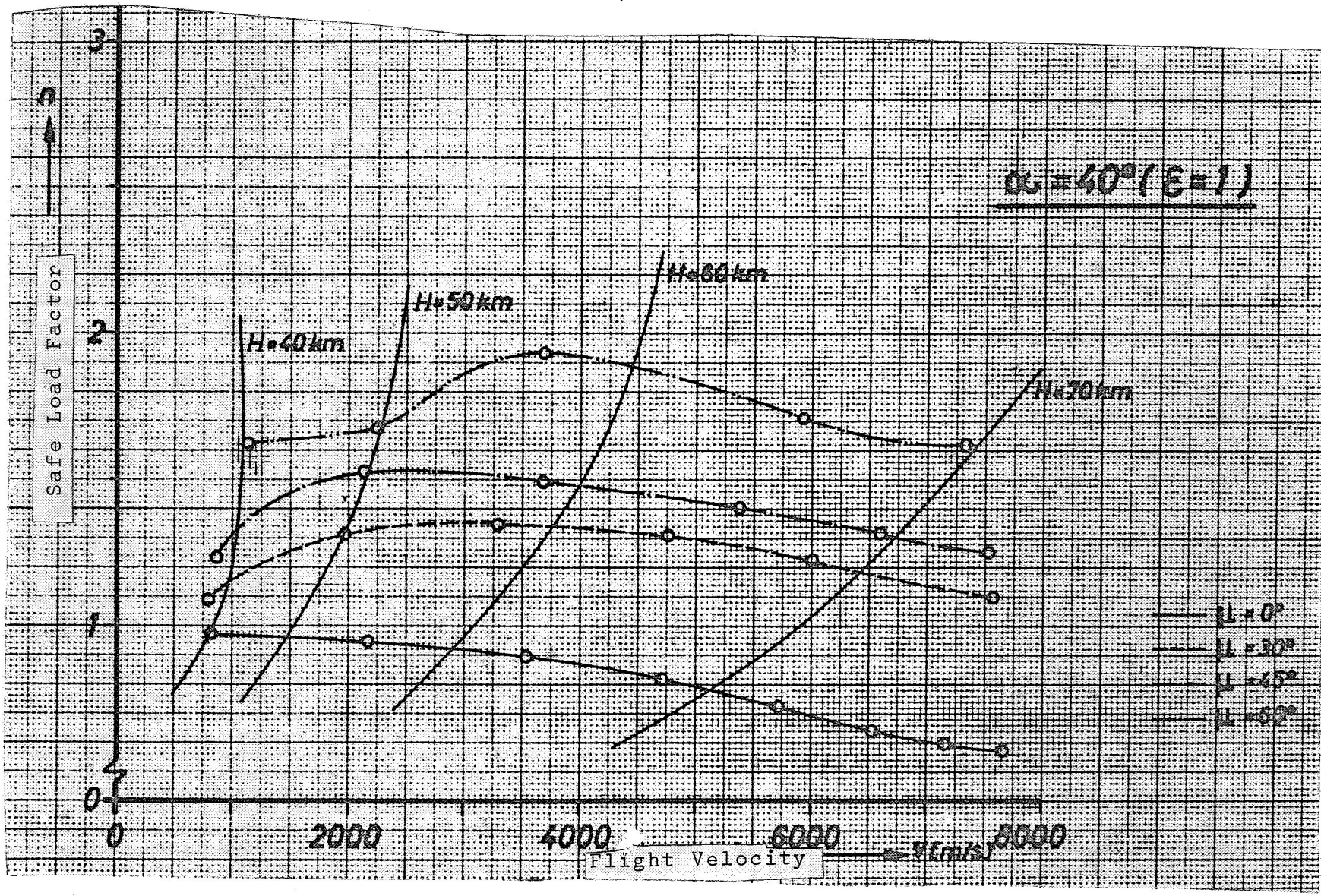

Figure 12. Safe Load Factor (Normal to Path)

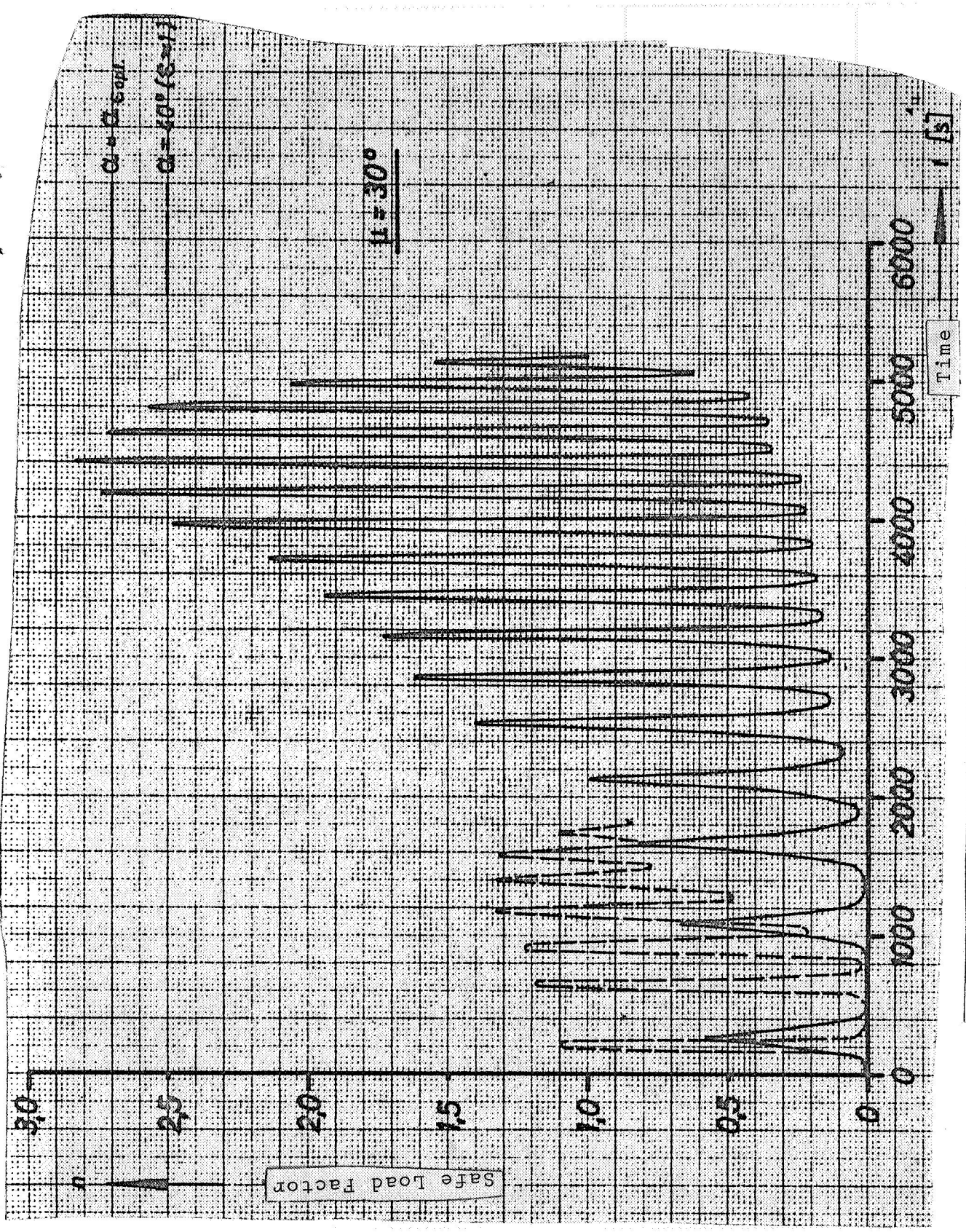

Figure 13. Safe Load Factor Time Curve (Normal to Path)

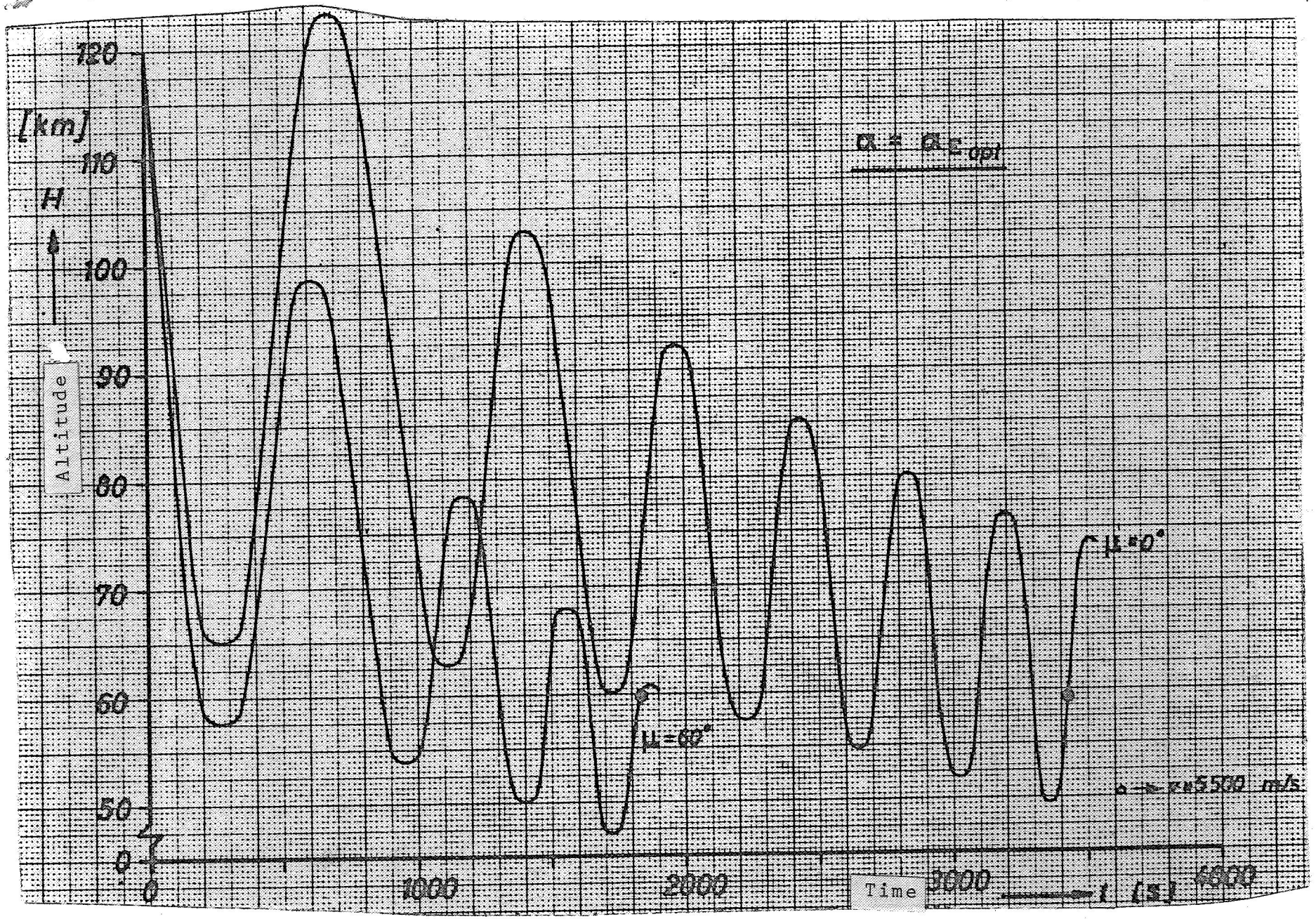

Figure 14. Time Curve for Flight Altitudes

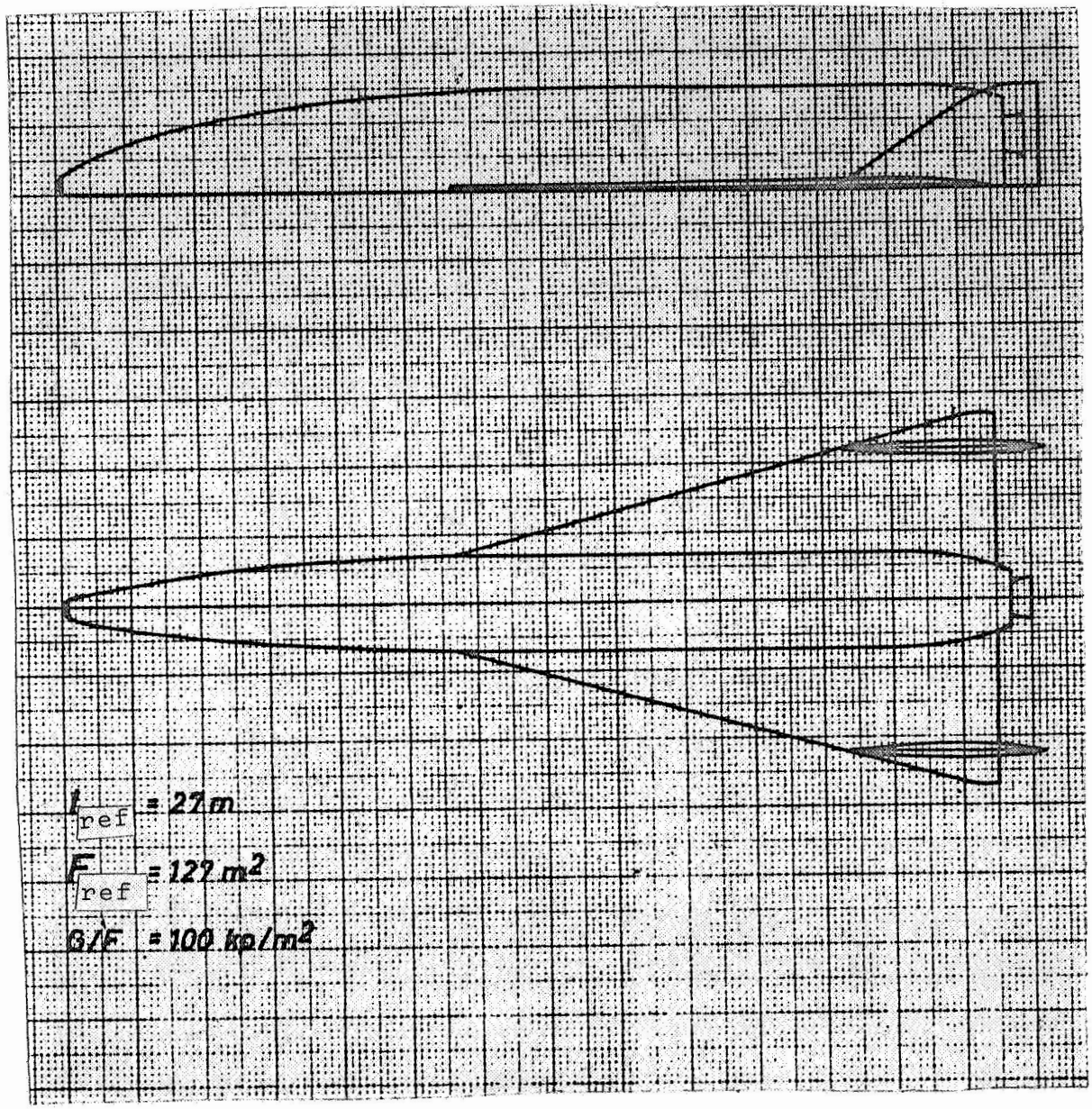

Figure 15. Space Transporter, Second Stage